Computational study of boron nitride nanotube synthesis: How catalyst morphology stabilizes the boron nitride bond

S. Riikonen,[1] A. S. Foster,[1,2] A. V. Krasheninnikov,[1,3] and R. M. Nieminen[1],*

[1]*COMP/Department of Applied Physics, Helsinki University of Technology, P.O. Box 1100, Helsinki FI-02015, Finland*
[2]*Department of Physics, Tampere University of Technology, P.O. Box 692, FI-33101 TUT Tampere, Finland*
[3]*Materials Physics Division, University of Helsinki, P.O. Box 43, Helsinki FI-00014, Finland*
(Received 13 May 2009; revised manuscript received 18 September 2009; published 13 October 2009)

In an attempt to understand why catalytic methods for the growth of boron nitride nanotubes work much worse than for their carbon counterparts, we use first-principles calculations to study the energetics of elemental reactions forming N_2, B_2, and BN molecules on an iron catalyst. We observe that the local morphology of a step edge present in our nanoparticle model stabilizes the boron nitride molecule with respect to B_2 due to the ability of the step edge to offer sites with different coordination simultaneously for nitrogen and boron. Our results emphasize the importance of atomic steps for a high yield chemical vapor deposition growth of BN nanotubes and may outline new directions for improving the efficiency of the method.

PACS number(s): 31.15.ae, 34.50.Lf, 36.40.Jn, 75.50.Bb

I. INTRODUCTION

Boron nitride nanotubes (BNNTs) consist of hexagonal graphiticlike sheet of alternating boron and nitrogen atoms rolled into a tube.[1–3] The structure of BNNTs is analogous to the more well-known (monatomic) carbon nanotubes (CNTs) but their physical properties are quite different from those of their carbon counterpart. The mechanical and wear-resistant properties of both materials are of the same impressive order (for example, the Young's modulus is in the terapascal range[4]) while the electronic properties of BNNTs can be more attractive. CNTs are either metals or semiconductors depending on their chirality while BNNTs are always semiconductors[5,6] with the gap (~5.5 eV) practically independent of the nanotube chirality and its diameter.[5] As hexagonal boron nitride (h-BN) is very resistant to oxidation,[7,8] BNNTs which inherit these properties are suitable for shielding and coating at the nanoscale. Despite these prospects, BNNTs have received very little attention compared to CNTs due to various difficulties in their reproducible and efficient synthesis.[9]

The fact that the BNNT consists of two different atomic species implies that the synthesis of BNNTs is more complicated than the synthesis of monatomic CNTs, as additional chemical reactions are possible. CNTs are typically synthesized from hydrocarbon precursors[10,11] and according to current theoretical understanding of the CNT formation process, individual carbon atoms diffuse in or on a metal nanoparticle, forming graphitic networks that eventually gives rise to the appearance of a CNT (see, e.g., Refs. 12–14). Assuming that these ideas are relevant to the growth of BNNTs, it becomes important to understand the factors that determine whether individual nitrogen and boron atoms diffusing on a catalytic surface result in the formation of BN structures, or N_2 molecules and B clusters.

In this paper, in an attempt to understand why catalytic methods for the growth of BNNTs work much worse than for their carbon counterparts, we use first-principles calculations to study the behavior of N_2, B_2, and BN molecules on an iron catalyst. Such molecules are the simplest systems involved

and the complete understanding of their behavior on the catalyst surface is a prerequisite to understanding the whole process. We assume an ideal situation, where the precursors used for producing BNNTs (and similar structures) are decomposed into individual boron and nitrogen atoms and deposited on the catalyst. We chose iron as the typical catalyst used in chemical vapor deposition (CVD) growth. We then investigate under which situations the BN formation becomes energetically favorable. We show that on a (110) close-packed surface of bcc iron, B_2 formation will dominate while at step edge regions, BN formation will be the most favorable reaction.

This paper is organized as follows: in Sec. II we first give a brief review of the synthesis methods of BNNTs and similar structures. In Sec. II F we explain the approximations and the computational approach we have chosen and how they can be justified. In Sec. III we discuss in detail the computational methods. In Sec. IV, we present our results and demonstrate how specific catalyst morphologies stabilize the BN bond. To better understand the underlying chemistry, in Sec. IV C we analyze the electronic structure of the adsorbed molecules. Finally in Sec. V, we discuss the implications of our results for BNNT synthesis on an iron catalyst.

II. SYNTHESIS OF BNNTs AND RELATED STRUCTURES

BNNTs have been synthesized with various methods and in a wide range of temperatures. Nearly all the methods show traces of metal particles but their role as a catalyst is far from clear. In this section, we give a brief overview of BNNT synthesis, with the emphasis on the role of catalysts if present in the synthesis method.

A. Arc discharge

BNNTs were synthesized with the arc-discharge method, using BN-packed tungsten anode and copper cathode.[1] Successively various anode and cathode materials, including hafnium diboride,[15] tantalum press filled with boron nitride,[16] and a mixture of boron, nickel, and cobalt[17] have

been used. Typically, amorphous particles have been observed at the BNNT tips[16] or encapsulated in BN cages.[15] These particles could be metallic (borides), implying a metal catalyzed synthesis[16] while the encapsulated material could also be BN and the synthesis would be noncatalytic.[15] A noncatalytic open-ended growth (involving no nanoparticles) has also been proposed.[17]

Keeping in mind that temperatures in the arc-discharge method reach beyond 3000 °C, it is probably not well suited for mass production of BNNTs.

B. Laser ablation

The laser-ablation method is based on the vapor-liquid-solid model[18] in which the target material is evaporated and precipitated from the vapor phase, eventually forming nanoparticles and solid, wirelike nanostructures. These are then carried by a gas flow to a collector.[18]

Yu *et al.*[19,20] used BN powder as the target ($T \sim 1200$ °C) and observed that adding small amounts of catalyst Ni and Co into the target, resulted in longer nanotubes of better quality that were more often single walled.[19] Metal particles were observed to encapsulate inside BN material and they were thought to play an important role in the synthesis.[20]

In other studies featuring higher temperatures[21,22] (2400–3000 °C), pure BN targets were used and BNNT growth from pure boron nanoparticles was observed.[21,22] In other laser-based techniques used for synthesizing BNNTs, the resulting product is typically collected directly from the target itself: Laude *et al.*[23] achieved BN dissociation by laser heating in low-pressure nitrogen atmosphere. This resulted in BNNTs and BN polyhedra that grew out of liquid boron.[23] Golberg *et al.*[2] heated cubic BN by laser[2] in diamond-anvil cell at high temperature and pressure, producing BNNTs directly from the liquid phase.[2] Ablation of BN by high-frequency laser in low-pressure nitrogen atmosphere,[24] produced BNNTs and BN "nanohorns."

C. Ball milling and annealing

Annealing methods have been used to produce BN nanowires, "nanobamboos" and BNNTs. These methods produce tubular BN structures by first milling the boron containing starting material into a fine powder during long times (typically ~ 24 h) and then annealing it at temperatures of ~ 1000–1200 °C in an inert[25] or nitrogen containing[26–30] atmosphere. As the starting material, h-BN (Refs. 25, 26, and 28) or pure boron powder[25,27,29,30] have been used. During the milling, the starting material can be activated,[30] by performing the milling in reactive atmospheres. Pressurized N_2 (Ref. 26) or ammonia gases[27,29,30] have been used for this purpose. Nanosized metal particles observed frequently in the samples come from the metal balls used in the milling process.

There seems to be no generally accepted scheme how nanotubes form in this synthesis method. Metallic nanoparticles were observed frequently in the samples and it was argued that they facilitate the growth of nanotubes[25,28] while it was concluded in other works that they are not

important.[29] Some authors simply state that their role is not clear.[26,27,30] In general, the nanotubes synthesized by these methods are of poor quality and the yields are very small, so the methods are not, at least at the present stage, very suitable for mass production of BNNTs.

Related to these methods is the work of Koi, Oku and co-workers[31–34] in which either hematite[31] or Fe_4N powder[32–34] together with boron powder was annealed in nitrogen atmosphere at ~ 1000 °C. Iron particles coated in BN layers,[31,32] BN nanowires,[32] hollow cages,[33] "nanobamboo" structures,[34] nanotubes, and "cup-stacked" nanotubes[33] were synthesized. In these works, the formation of BN layers in the reactions involving Fe_4N has been described in two different ways: either Fe_4N and Fe_2B become liquid, boron segregates on the nanoparticle surface and reacts with the N_2 atmosphere,[32] or an amorphous boron layer on the Fe_4N is converted to BN as the Fe_4N is reduced from nitrogen.[34]

D. Chemical vapor deposition

In a CVD method, one or more volatile precursors react and decompose on the catalyst to form the desired compound. CVD methods for producing BN filaments and BNNTs have been utilized in several works.[35–41]

Gleize *et al.*[35] used diborane and ammonia or N_2 gases as the boron and nitrogen containing precursors. These were deposited on various boride surfaces (including Zr, Hf, Ti, V, Nb, and Ta borides) at a temperature of 1100 °C. It was observed that diborane did not play any role in the tubule growth (diborane and ammonia formed amorphous BN only) but the boron in the reaction came from the boride catalyst itself.[35] The boride then acted both as a catalyst and as a reactant for the tubules. Successive studies using similar temperatures have made the same observation.

Lourie *et al.*[37] deposited borazine on cobalt, nickel, and nickel boride catalyst particles and concluded that the boride catalyst gave the best results. Huo *et al.*[39,41] used for the nitrogen containing precursor a mixture of ammonia and nitrogen gas. The boron source was again the catalyst itself which consisted of iron boride nanoparticles.

In another study[40] nickel boride nanoparticles supported on alumina (in order to avoid nanoparticle agglomeration) with ammonia and nitrogen were used. BNNTs were observed to grow out of the nickel boride nanoparticles at $T = 1100$–1300 °C, while no "nanobamboo" structures were observed (anglomeration was avoided).

Ma *et al.*[38] emphasized that CVD using metal catalysts must be difficult due to the poor wetting property of BN with metals. For this reason they used melamine diborate to create a metal-free B-N-O precursor.[38,42,43] This precursor then reacted with N_2 at 1200–1700 °C. Tip growth of multiwalled BNNTs from amorphous B-N-O clusters was observed.[38] The synthesis was explained by condensation of BN from the vapor phase into the B-N-O particles[38] or either by reduction of B_2O_3 vapor.[42]

Borazine and similar molecules have been used in CVD to produce BN nanotubes. Shelimov and Moskovits[36] created BN nanotubes by depositing 2,4,6-trichloroborazine on aluminum oxide at a temperature of 750 °C. These kinds

of methods are based on the thermal decomposition (pyrolysis) of borazine and similar molecules on surfaces[44] and there is a direct connection to the CVD synthesis of h-BN thin films, a theme that has been reviewed by Paine and Narula.[7]

E. Other

Other methods include the substitution of carbon atoms in CNTs by boron and nitrogen,[45–48] reduction-nitridation reactions,[49] and boric acid reacting with activated carbon.[50] Finally, the most successful method up to date for synthesizing BNNTs is by Tang and co-workers.[9,51,52]

In the method of Tang *et al.*,[9,51,52] boric oxide vapor was created *in situ* and reacted with ammonia at temperatures $T \geq 1100$ °C. Boric oxide was created from magnesium oxide and boron powder. Magnesium was also thought to act as a catalyst in the reduction of boric oxide into boron nitride.[51] This method seems to be related to the "classical high-temperature" methods to produce bulk h-BN,[7] where the formation of h-BN is attributed to the gas forming property of the undesired elements (oxygen) and the thermodynamical stability of h-BN.[7]

By this method, boron and nitrogen could be converted into BNNTs by an efficiency of 40% (Ref. [51]) and hundreds of milligrams of BNNTs were produced. Most of the nanotubes were open ended, although some encapsulated material was found in the samples.[51] Liquid-phase magnesium drops could have catalyzed the reaction but in this case they were evaporated in the final process.[51] The quantity and quality of BNNTs depended strongly on the temperature: below 1100 °C, quality was better, but yield was small.[52] Increasing the temperature, increased the yield, but tube diameter started to grow and BN flakes were formed when temperature was beyond 1250 °C.[52] Adding FeO to the initial MgO powder, solved this problem and BNNTs could be produced up to 1700 °C.[52] The growth then seemed to be catalytic.[52]

F. Common features and the role of catalyst as the simulation challenge

As evident from this brief review, BNNTs can be synthesized by various methods and in nearly all of them, metal particles which may have catalytic activity, are present. However, the role of metal catalysts in BNNT growth is not well understood.

In the CVD methods and when metal catalysts are involved, it seems to be important to use borides instead of pure metals. Borides are able to dissolve boron and nitrogen at the same time[35] while the solubility of boron, for example, in iron is known to be very small.[53] On the other hand, borides likely provide boron atoms during the BNNT growth,[35] so they act both as the catalyst and the reactant itself, which is conceptually very different from the case of CNT synthesis.

In methods using borazine and similar molecules, we must keep in mind that these molecules already contain the desired boron nitride bonds. We can then imagine that the pyrolysis of these molecules in temperatures of $T \sim 800$ °C is used rather to remove the hydrogen atoms than breaking the boron nitride bonds. This synthesis can then be conceptually quite different from the other synthesis methods. Finally, in the state-of-the-art method (Tang, Golberg, Zhi, and others), the catalytic role of iron and magnesium used in the process is not fully understood.

All these synthesis methods pose interesting challenges for theoretical calculations. However, to our knowledge only a single *ab initio* study on BNNT synthesis has been published.[54] In that study, the noncatalytic growth of BNNTs was considered and it was shown that open-ended growth of single-walled armchair BNNTs is, in principle, possible.[54]

Modeling a catalytic process is a very challenging problem. Many of the *ab initio* studies in this field concentrate in studying situations where the catalyst is reactive enough to dissociate a precursor while not being too reactive to block the synthesis.[55] A typical example of a thoroughly studied catalytic synthesis process is the ammonia synthesis and its rate-limiting step, the N_2 dissociation.[56]

In this work, we study the adsorption energies, reaction energies, and some reaction barriers for simple boron and nitrogen containing molecules on a catalyst. We are trying to find reasons why BNNT synthesis on transition metals has proven to be so difficult and if the boron nitride formation could be made energetically favorable. We do this by studying the stability of the boron nitride bond on iron. This can be seen as a natural first step before addressing more complicated issues and catalysts (such as borides).

Our computational setup mimics the CVD synthesis. We assume that the precursors (not defining them) have dissociated and donated B and N atoms on the catalyst. In the simulations, we then adsorb individual B and N atoms on the surface and calculate the reaction energetics when these adsorbed atoms (X^* and Y^*) form adsorbed molecular species (XY^*).

Thinking in terms of this simplified model of CVD synthesis it is easy to understand why boron nitride structures can be much more difficult to form than pure carbon structures; in the carbon case and looking at the most simple molecules, we have only carbon atoms involved in the reactions, i.e., $XY^* = C_2^*$ while in the boron nitride case we have several competing diatomic molecules, i.e., $XY^* = N_2^*$, B_2^*, or BN^*.

As the adsorbed boron and nitrogen atoms react on the catalyst surface, complicated surface species might form, for example, boron clusters, boron-iron clusters, BN molecules and chains and clusters consisting of both boron and nitrogen, etc. If our goal is to understand the problems in BNNT synthesis in such a complex situation, a good first step is to study the most simple surface species, i.e., the adsorbed diatomic molecules that can be formed with adsorbed B and N. If, by studying these simple diatomic molecules, we find situations where the catalyst "promotes" the formation of BN^* molecule instead of N_2^* and B_2^* molecules, this should have consequences in more realistic situations as well; the BN molecules formed on the catalyst surface might act as seeds for further boron nitride nucleation and successive nanotube growth.

Finally, we emphasize that in this work we are interested in the theoretical aspect of the boron nitride bond stabilization. Modeling realistic reaction conditions is out of the

scope of the present work. This would typically call for the calculation of several adsorption and coadsorption configurations, coverages, and reaction paths.[57] We also concentrate in the small molecular species B_xN_y, where $x, y = \{0, 1\}$. Considering bigger molecules at the DFT level becomes computationally very difficult as the number of possible molecules increases rapidly as a function of the number of atoms.

III. METHODS

A. General concepts

In *ab initio* calculations, realistic catalyst nanoparticles are frequently modeled by slabs in supercell geometry, consisting of 3–6 atomic layers of catalyst and a sufficient amount of vacuum (>10 Å) between the slabs. The slab usually contains a step edge in order to model a realistic nanoparticle with active sites.[13,56,58]

In the following, we assume that two adsorbates, X^* and Y^*, are far away from each other on the surface and we bring them together to form a new adsorbate species XY^*. The energy for this reaction $X^* + Y^* \rightarrow XY^*$ can be calculated as follows:

$$\Delta E = [E(XY^*) + E_0] - [E(X^*) + E(Y^*)], \quad (1)$$

where $E(X^*)$ is the energy of the adsorbed surface species X^* and E_0 is the energy of a surface unit cell without adsorbates. We manipulate Eq. (1) as follows:

$$\begin{aligned}\Delta E &= [E(XY^*) + E_0] - [E(X^*) + E(Y^*)] \\ &= [E(XY^*) - E_0] - \{[E(X^*) - E_0] + [E(Y^*) - E_0]\} \\ &= E_s(XY^*) - [E_s(X^*) + E_s(Y^*)] \quad (2)\end{aligned}$$

in the last line of the equation, we have used energy values E_s defined as

$$E_s(X^*) = E(X^*) - E_0. \quad (3)$$

We observe from Eq. (2) that using "shifted" energy values E_s defined in Eq. (3), we can calculate the reaction energy for a reaction $X^* + Y^* \rightarrow XY^*$ on the surface with the simple formula

$$\Delta E = E_s(XY^*) - [E_s(X^*) + E_s(Y^*)]. \quad (4)$$

In Sec. IV, we tabulate values of E_s in different parts of the catalyst surface (terrace and edge) and then use these tabulated values to calculate reaction energetics using Eq. (4).

Using the same notation, the adsorption energy can be written as follows:

$$E_{ads} = E(X^*) - E(X) - E_0 = E_s(X^*) - E(X) \quad (5)$$

and the dissociative adsorption energy, i.e., energy for reaction $XY(g) \rightarrow X^* + Y^*$ as

$$E_{dis} = E_s(X^*) + E_s(Y^*) - E(XY), \quad (6)$$

where $E(X)$ is the energy of the molecular species in the gas phase.

B. Computational methods

The calculations were performed with programs in the framework of the density-functional theory (DFT), as imple-

mented in two different codes, SIESTA and VASP. The SIESTA code[59,60] uses pseudoatomic orbitals as its basis set while VASP (Refs. [61–63]) is based on plane waves. SIESTA relies on the pseudopotential method to describe the core electrons while projected augmented waves (PAWs) (Ref. [64]) can be used in VASP. All calculations were done with periodic boundary conditions, collinear spin, and using the Perdew-Burke-Ernzerhof general gradient approximation.[65] We use the Monkhorst-Pack (MP) sampling[66] of the Brillouin zone in calculations involving the slab. As we are using different k-point samplings, we will indicate the fineness of the M $\times$ N Brillouin-zone sampling also with the area of the reciprocal space per one sampled k-point (A_{BZ}). In this work, preliminary calculations were typically done with SIESTA while the final energies were always calculated with VASP. Due to the more systematic control of accuracy in the VASP code, we use it as a benchmark for the more computationally efficient SIESTA code. Nudged elastic band (NEB) calculations[67] for reaction barriers were performed entirely with VASP.

1. SIESTA

In SIESTA calculations, Troullier-Martins[68] scalar-relativistic pseudopotentials, with nonlinear core corrections were used. The density of the real-space grid was defined by a corresponding plane-wave cutoff of $\sim$350 Ry and the effective density of the grid was further increased using a grid cell sampling of 12 points. The basis set used by SIESTA consists of numerical pseudoatomic orbitals.[59,69,70] These orbitals are obtained from the same atomic calculation that is used to generate the pseudopotentials (thus the name "pseudoatomic"). The cutoff radii and the amount of confinement of these orbitals can be defined either by the cutoff radii (r_c) or by the "energy-shift" parameter (E_{shift}), larger energy shift corresponding to increasingly confined orbitals and smaller cutoff radii.[71] In SIESTA, a typical basis set is the double-ζ polarized (DZP) that consists of doubled atomic orbitals and an extra set of polarization orbitals created using perturbation theory. A typical value for the E_{shift} parameter in solids is $\sim$200 meV.

For the molecular species in this study, we used the DZP basis set and $E_{shift} = 150$ meV. In the case of boron this leads to a basis set with doubled $2s$ and $2p$ orbitals plus an additional set of $3d$ orbitals. The total amount of orbitals is then 13 for one boron atom. The cutoff radii defined using the energy shift for boron are 2.7 Å ($2s$), 3.3 Å ($2p$), and 3.3 Å ($3d$). For nitrogen the cutoff radii from the energy shift are 2.0 Å ($2s$), 2.5 Å ($2p$), and 2.5 Å ($3d$).

SIESTA has earlier been used to simulate iron nanoparticles[72,73] using both the SZSP and DZSP basis sets. The SZSP consist of $3d$, $4s$, and $4p$ orbitals while in DZSP $3d$ and $4s$ orbitals are doubled. In Refs. [72] and [73] an explicit confinement radius of $r_c = 2.3$ Å for both SZSP and DZSP basis sets was used and it was demonstrated that these basis sets with $r_c = 2.3$ Å produced very well the properties of iron, including the magnetism.[73] However, in the present case and while studying chemisorption of molecules on iron surface, we prefer longer cutoff radii and thus use a SZSP basis with $E_{shift} = 150$ meV to define the cutoff radii of the

orbitals. This way, the cutoff radii for the iron orbitals are 2.41 Å ($3d$), 3.9 Å ($4s$), and 3.9 ($4p$). In our basis set, all atoms have then basis orbitals that extend at least up to 2.5 Å and some of them up to 3.9 Å.

We represent the surface by a three-layer iron slab, with the vacuum between neighboring slabs being always $\sim$14 Å. When placing a molecule on top of this slab, only the molecule and the top iron layer are allowed to move during the conjugate gradient (CG) geometry optimization. In order to speed up the calculation, the parameter adjusting the convergence of the self-consistency cycle is increased to 10^{-3}. This will affect the accuracy of the forces, so we simultaneously increase the force tolerance criterion for stopping the CG relaxation to 0.1 eV/Å. MP sampling is chosen to be 1×2, corresponding to $A_{BZ}=0.15$ Å^{-2}. The idea of this approximative calculation is to get a sound initial guess for the next stage in which we use the VASP code.

2. VASP

In VASP, PAWs were used. The cutoff energy of the plane-wave basis set was always 420 eV. We represent the surface by a four-layer iron slab, with the vacuum between neighboring slabs always $\sim$14 Å. Only the bottom layer is fixed to the bulk positions during the CG relaxation. Mixing scheme in the electronic relaxation is the Methfessel-Paxton method[74] of order 1. In a first stage, the system is relaxed using a 1×2 MP sampling, which corresponds to $A_{BZ}=0.16$ Å^{-2}. When needed, the CG relaxation is automatically started again or until the forces have converged to a minimum value of 0.01 eV/Å. After this, the relaxation is continued with MP sampling of 3×5, corresponding to $A_{BZ}=0.02$ Å^{-2} and CG relaxation is restarted if needed. This way we are able to reach a maximum force residual of $\approx$0.02 eV/Å. In all calculations special Davidson block iteration scheme was used and symmetries of the adsorption geometries were not utilized. The standard "normal" accuracy was used.

In the case of NEB calculations, and due to the large number of atoms we are considering, only three image points (plus the two fixed points) were used. In general, we observed that NEB calculations with large surface slabs can be tedious; some configurations at the lowest-energy path could bring down their total energies by shifting the iron layers in a collective movement and this way change the relative position of the adsorbant molecule to energetically more favorable site. To avoid this unphysical situation, we fixed the lowermost layers and relaxed only the topmost iron layer and the adsorbed molecule during the NEB calculations. This must exaggerate the reaction barriers but we believe that this approximation should be valid for comparative estimations on the order of magnitude of the reaction barriers and for the observation of rate-limiting steps.

C. Adsorption sites

The unit cell used in our calculations is depicted in Fig. 1. The coordinates of the iron surface atoms were always scaled to the computational lattice constant, which for SIESTA and VASP were 2.89 and 2.83 Å, respectively [the experimental
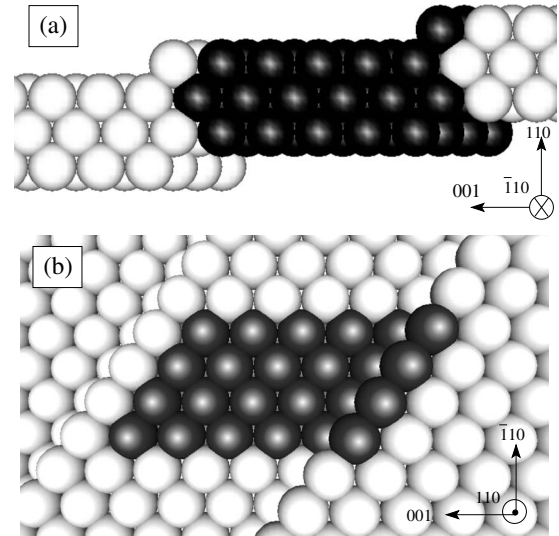

FIG. 1. BCC iron (110) surface with a step. The unit cell which was used in our calculations is indicated by atoms with black color. Unit cell in this figure shows a three-layer slab. Lengths of the unit-cell sides are 9.8 and 15.6 Å.

value of the lattice constant for BCC iron being 2.87 Å (Ref. 75)]. The unit cell of Fig. 1 has either 68 (three-layer slab) or 92 (four-layer slab) atoms. Using a large enough unit cell, including both flat and stepped regions, allows us to perform a comparative study of the adsorption energetics near and far away from the step. A large unit cell should also allow for more realistic relaxation of the topmost iron atoms. We will now explain our strategy for searching the optimal geometries of adsorbed molecules on the surface.

In Fig. 2(a) we are considering nine different sites. Sites (1–3) are in a close-packed region of the iron surface. The remaining sites are either on top or in the vicinity of the step edge. In Fig. 2(b) different positions of a diatomic molecule have been considered. For each position, a set of numbers has been associated. This nomenclature corresponds to the site numbering of Fig. 2(a). The positions together with the associated site numbers constitute the systematic search for the adsorption site. This procedure is more clearly understood with the example of the BN molecule: at the begin-
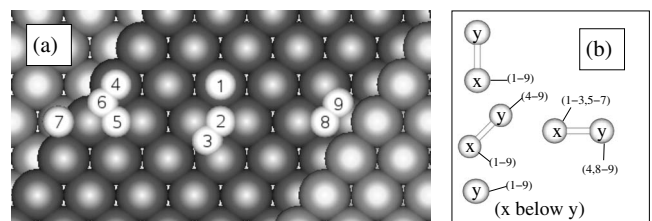

FIG. 2. (a) Different sites tried out for chemisorption of molecules in the stepped iron slab. Sites (1–3) correspond to flat surface while sites (4–9) are in the vicinity of the step edge. Sites 1 and 4 correspond to top sites, 2, 5, and 8 to "hollow" sites, and 3, 6, 7, and 9 to "bridge" sites. (b) Different positions tried out for chemisorption of molecules. The positions in panel (b) have the same perspective as the surface slab in panel (a). How these positions and sites are used to search for the optimal adsorption site, see Sec. III C.
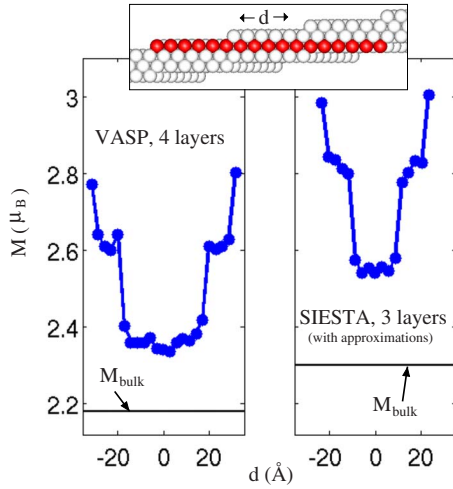
FIG. 3. (Color online) Magnetic profile of the stepped iron slab of Figs. 1 and 2, when moving along atoms indicated by red color in the topmost panel. Left panel: magnetic profile using VASP and a four-layer slab. Right panel: magnetic profile using SIESTA with three-layer slab and some approximations (see Sec. III B 1). Bulk magnetism (M_{bulk}) has been indicated by a solid line for both SIESTA and VASP.

ning, we will assign the labels x and y used in Fig. 2(b) as (x=B, y=N). After this, the BN molecule would be positioned according to each rotation in Fig. 2(b) and for each rotation, the atom (x=B) is placed on the sites, indicated by the numbers for the x label in Fig. 2(b). As BN has two different atomic species, we must repeat the procedure with (x=N, y=B). For a diatomic molecule with two different species, this accounts for 66 trial configurations and for a molecule consisting of one species only, half of that.

We perform the systematic search described above for each atom (N and B) and for each molecule (N_2, B_2, and BN), using the approximative SIESTA calculations. During this first stage, quite many of the different trial configurations relax into the same energy minimum. Some five to ten of the most favorable adsorption geometries are then recalculated with VASP for final results.

IV. RESULTS

A. Iron slab properties

Magnetism is known to play an important role in iron nanoparticles. Typically, the magnetic moment in the nanoparticle surface is increased and deeper inside the nanopar-
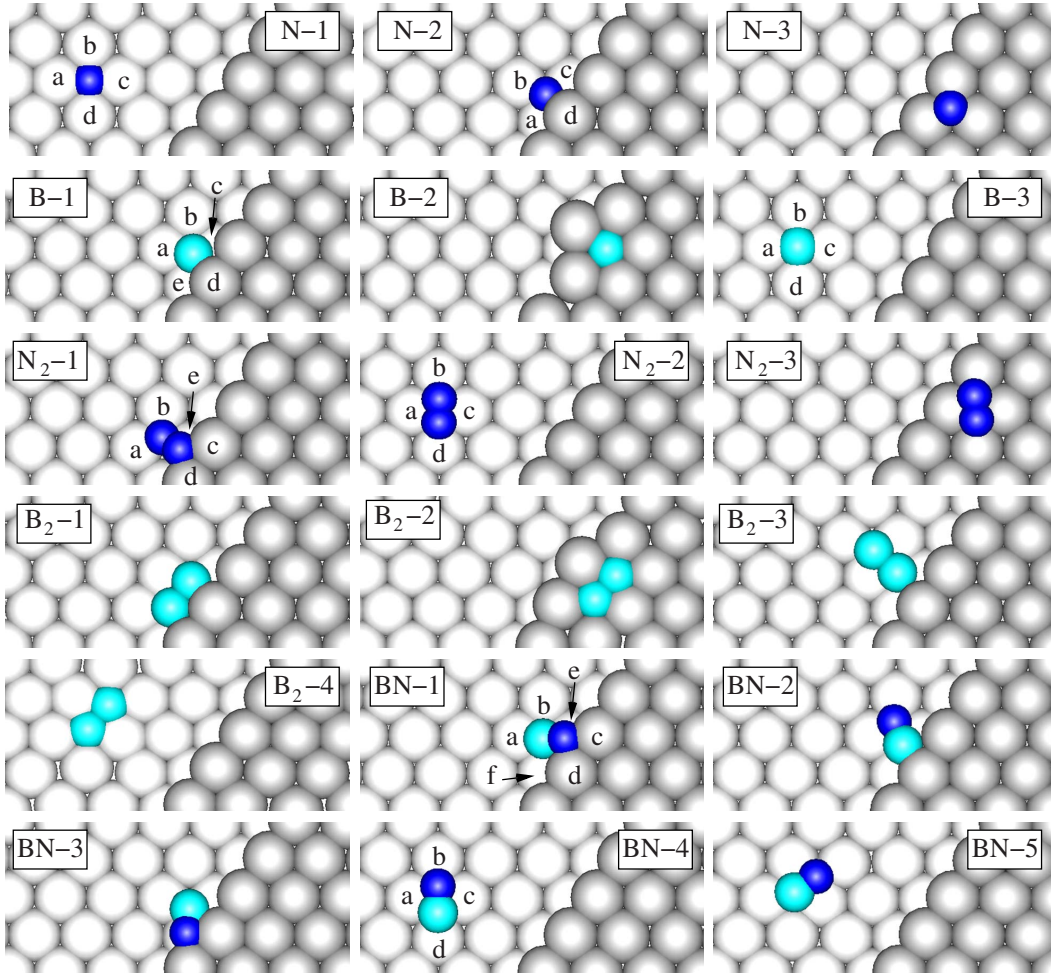

FIG. 4. (Color online) Some of the most stable geometries for B_2, BN, and N_2 molecules and the B and N atoms on the iron surface. Different geometries are tagged with the same labels as in Table I. In the case of BN, magenta (blue) corresponds to boron (nitrogen).

TABLE I. Adsorption energies E_{ads} and energies E_s [see Eq. (3)]. Values of E_s can be used directly to calculate reaction energies on the surface by using Eq. (4). Values for N_2, BN, and B_2 molecules and N and B atoms in different adsorption geometries on the iron surface have been tabulated. Bond lengths (BL) on the adsorbant and in the vacuum (in parenthesis) are listed. Sites and geometries have the same labels as in Figs. 4–8 and in Tables II and III.

Adsorbate	E_{ads} (eV)	E_s (eV)	BL (Å)
N-1	−6.6	−9.7	
N-2	−6.4	−9.5	
N-3	−6.2	−9.3	
N-4	−5.9	−9	
B-1	−6.7	−7	
B-2	−6.6	−6.9	
B-3	−6.3	−6.6	
N_2-1	−1.2	−17.7	1.33(1.12)
N_2-2	−1.1	−17.6	1.28
N_2-3	−1.1	−17.6	1.29
BN-1	−8.1	−16.9	1.4(1.34)
BN-2	−7.8	−16.5	1.39
BN-3	−7.7	−16.4	1.43
BN-4	−7.3	−16.1	1.38
BN-5	−7.3	−16.1	1.42
B_2-1	−9.9	−14.1	1.78(1.62)
B_2-2	−9.6	−13.8	1.73
B_2-3	−9.3	−13.5	1.76
B_2-4	−9.3	−13.5	1.77

TABLE II. Adsorption energies E_{ads} for N_2, BN, and B_2 molecules and N and B atoms in different parts of the iron surface. Terrace region (t) corresponds to sites (1–3), edge region (e) to sites (4–9), and the whole surface ($t+e$) to all sites in Fig. 2. The energy difference when moving the atom from the optimal site at the terrace (t) to the optimal site in the edge (e) is calculated in the last column. All energies listed are in the units of eV.

Adsorbate	$E_{ads}(t)$	$E_{ads}(e)$	$E_{ads}(t+e)$	$E_{ads}(e)-E_{ads}(t)$
N^*	−6.6	−6.4	−6.6	0.2
B^*	−6.3	−6.7	−6.7	−0.5
N_2^*	−1.1	−1.2	−1.2	−0.1
NB^*	−7.3	−8.1	−8.1	−0.8
B_2^*	−9.3	−9.9	−9.9	−0.7

consistent with VASP.

In general, the magnetic moment at the top surface layer is enhanced by 20–30 % when compared to the bulk values. This is consistent with the behavior of magnetism in iron nanoparticles[73] and on transition-metal surfaces.[76]

B. Reactions of molecules on the catalyst

As we explained in Sec. II F where we motivated our computational approach, we concentrate on the most simple molecules that can be formed from N^* and B^* that are adsorbed on the catalyst surface and look directly at the energetic balance of the reactions $X^*+Y^* \rightarrow XY^*$ that form BN^*, N_2^*, and B_2^*. When calculating the reaction energies, we use Eq. (4) and tabulated values of E_s.

The optimal positions for adsorbed N, B, N_2, B_2, and BN molecules have been found using the approach described in Sec. III C and they are illustrated in Fig. 4. The indices given to these molecular geometries (B_2-1, B_2-2, etc.) are the same as used in Tables I and III and in the density of state plots in Fig. 6. The main results of the adsorption energetics on the iron slab have been collected in Table III. There the energetics have been categorized according to different regions of the iron slab of Fig. 2: the "terrace" corresponds to sites (1–3), "edge" region to sites (4–9) and the "terrace and edge" to all sites in Fig. 2. In each class the energetically most favorable surface geometry has been considered. In the terrace and edge column, the atoms are free to choose either terrace or edge sites (whichever is favorable), leading to different values than in edge and terrace rows.

From the results of Tables II and III, we can conclude the following: (1) the reaction $N^*+N^* \rightarrow N_2^*$ is unfavorable in every region of the surface, (2) in the terrace, the reaction $B^*+B^* \rightarrow B_2^*$ is the most favorable, (3) in the edge region, $B^*+N^* \rightarrow BN^*$ is the most favorable reaction and (4) in a situation where both terrace and edges are available, BN formation is still slightly more favorable than B_2 formation. (5) All the atoms and molecules (with the exception of the nitrogen atom) prefer to populate the step edge.

Energy barriers have been calculated along a few reaction paths for reactions $X^*+Y^* \rightarrow XY^*$ involving boron and nitrogen both at the terrace and at the step edge. The reaction barriers and some atomic configurations along the lowest-

ticle, the magnetic moment approaches that of bulk iron. The central atom of small nanoparticles might even obtain a minority spin.[73]

To test for this gradual change in magnetism when approaching the nanoparticle surface, we have plotted the magnetic profiles of the slabs used in this work in Fig. 3. In the case of SIESTA and VASP we have used the approximations described in Sec. III B. For SIESTA, we obtain a bulk magnetic moment of $2.3\mu_B$. Going from the center of the slab toward surface, the magnetic moment varies from 2.5 up to $3.0\mu_B$. For VASP, the bulk magnetic moment is $2.18\mu_B$ and in the slab it varies from 2.3 to $2.8\mu_B$. The experimental value for iron bulk magnetic moment is $2.2\mu_B$.[75] In both cases, the atoms at the step edge obtain the highest magnetic moment. In Fig. 3, the magnetic profiles start from d ≈ -30 Å with the high magnetic moment of the step edge atom. The magnetic moment is lowered by $\approx 0.2\mu_B$ for atoms residing at the terrace. As we move under the terrace, magnetic moment is lowered again approximately by the same amount. SIESTA, with the SZSP basis set and the approximations described in Sec. III B, gives slightly exaggerated magnetic moments (by $\approx 0.2\mu_B$ when compared to VASP) but the overall behavior is

TABLE III. Reaction energies (eV) of some reactions on the iron surface in different regions. Terrace corresponds to sites (1–3), edge to sites (4–9), and the whole surface to all sites in Fig. 2. The adsorbate geometries that are used to calculate the energy for reaction $X^* + Y^* \rightarrow XY^*$ are indicated in parenthesis. Geometries are tagged with the same labels (N-1, N-2, etc.) as in Table I and Fig. 4. Reaction energies are calculated by taking the corresponding energies E_s from Table I and using Eq. (4). (Note: high cost for the reaction in the fourth row is due to forcing the very unfavorable N_2 formation).

Reaction	ΔE (terrace)	ΔE (edge)	ΔE (terrace and edge)
$2N^* \rightarrow N_2^*$	1.7 $[2(N\text{-}1) \rightarrow N_2\text{-}2]$	1.3 $[2(N\text{-}2) \rightarrow N_2\text{-}1]$	1.6 $[2(N\text{-}1) \rightarrow N_2\text{-}1]$
$2B^* \rightarrow B_2^*$	-0.4 $[2(B\text{-}3) \rightarrow B_2\text{-}4]$	-0.1 $[2(B\text{-}1) \rightarrow B_2\text{-}1]$	-0.1 $[2(B\text{-}1) \rightarrow B_2\text{-}1]$
$B^* + N^* \rightarrow BN^*$	0.1 $[(B\text{-}3)+(N\text{-}1) \rightarrow BN\text{-}4]$	-0.3 $[(N\text{-}2)+(B\text{-}1) \rightarrow BN\text{-}1]$	-0.2 $[(N\text{-}1)+(B\text{-}1) \rightarrow BN\text{-}1]$
$2N^* + 2B^* \rightarrow N_2^* + B_2^*$	1.3	1.2	1.5
$2N^* + 2B^* \rightarrow 2NB^*$	0.2	-0.6	-0.4

energy path have been illustrated in Fig. 5. From Fig. 5 we can see that the energy barriers for competing reactions $B^* + B^* \rightarrow B_2^*$ and $B^* + N^* \rightarrow BN^*$ have the same order of magnitude in both at the terrace and at the step edge. No rate-limiting steps are observed.

Next we will take a detailed look at the geometries, compare some of them to earlier computational results and finally, based on the detailed analysis of the geometries we give a simple explanation why BN formations is so favorable at the step edge. We start by looking at the adsorption geometries of individual nitrogen and boron atoms.

1. Adsorption of N

In the adsorption geometry N-1 of Fig. 4, changes in the positions of surface iron atoms surrounding the adsorbed nitrogen are observed. In order to quantify these changes, we have labeled some of the atoms with letters a,b,c, and d. The distance from the adsorbed N atom to the neighboring iron atoms a and c (b and d) is 1.79(1.96) Å. Iron atoms have moved in order to create a fourfold site for the N atom by contracting the distance b-d by ∼5% and expanding distance a-c by ∼20%. The N atom is now almost completely incor-

porated in the first iron layer and its distance from the plane formed by atoms a, b, c, and d is only 0.5 Å while its distance to the iron atom lying directly below is 2.47 Å. The rather big unit cell we are using in our calculations has made it possible for the iron atoms to "give way" for the nitrogen atom and to adsorb deeply into the adsorbant at approximately fourfold symmetric site. In geometry N-2, the nitrogen atom has very similar coordination to N-1. Now nitrogen has found a fourfold site by taking advantage of the iron atoms at the step edge. Three of the neighbor iron atoms (a, b, and c) reside in the terrace while one of them (d) sits in the step edge. The distances of nitrogen to the nearest-neighbor iron atoms are (a) 1.87, (b) 1.90, (c) 1.86, and (d) 1.91 Å. Breaking the trend a bit, geometry N-3 prefers a threefold site. This must be related to the fact that it is in contact with two step-edge atoms and so the chemical environment and charge transfer must be different at this site.

Based on the geometries N-1, N-2, and N-3 we can conclude that, within the unit cell used in this study, nitrogen prefers threefold or fourfold sites with iron. Near the step edge there is no need to adsorb deeply into the iron layer in order to gain this desired coordination with iron. This is particularly true for geometry N-2 as it can easily have a four-
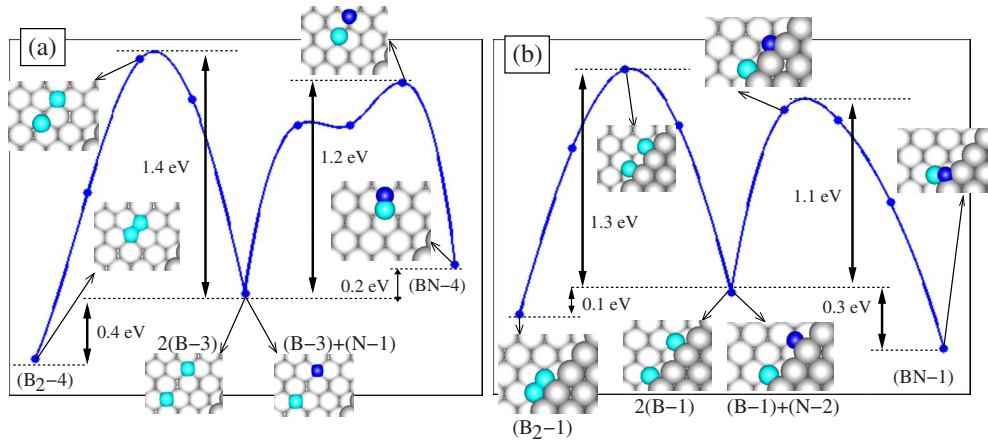

FIG. 5. (Color online) Reaction barriers along a few reaction paths for (a) reactions at the terrace ($2(B\text{-}3) \rightarrow B_2\text{-}4$ and $[(B\text{-}3)+(N\text{-}1) \rightarrow BN\text{-}4]$ and for (b) reactions at the step edge $[2(B\text{-}1) \rightarrow B_2\text{-}1$ and $(N\text{-}2)+(B\text{-}1) \rightarrow BN\text{-}1]$. The zero of energy for reactions $X^* + Y^* \rightarrow XY^*$ is fixed at the energy $E(X^* + Y^*)$, where both X and Y are at the same unit cell. The zero of energy for competing reactions forming B_2 and BN are set at the same value in order to make the comparison of energy barriers easier. The slightly higher (≈ 0.1 eV) energy cost for reaction $[(B\text{-}3)+(N\text{-}1) \rightarrow BN\text{-}4]$ than reported in Table III results from placing the N and B atoms in the same unit cell.

fold coordination with iron due to the step edge morphology. The energy differences between different nitrogen atom sites are not that big. From Table I, they are on the order of ~0.2 eV. From the point of view of catalytic synthesis involving nitrogen atoms, we could argue that having more step edges than flat terrace areas on the surface is beneficial, as the adsorption of nitrogen very deeply into the iron layer can be avoided.

In Ref. 77 nitrogen adsorption on Fe(111), (100), and (110) has been studied using DFT calculations. It was found that on Fe(100), nitrogen prefers a fourfold symmetric site. In the case of Fe(110), nitrogen was found to prefer a threefold site but the unit cell used in that case was very small and only the first layer of iron atoms was allowed to relax. It was also reported that calculated adsorption energies for Fe(111) and Fe(110) were smaller than for Fe(100), probably due to the lack of available fourfold symmetric sites. In our case, an approximately fourfold symmetric site is created in the Fe(110) surface by movement of iron atoms and the site created this way starts to resemble the one that exists in the Fe(100) surface. It is also noted in Ref. 77 that the reconstruction of iron surfaces due to nitrogen adsorption most likely consist of geometries very similar to the one observed in Fe(100).

We also calculated a configuration where the N atom is adsorbed into a threefold site on the terrace (not shown in the figures). The adsorption of nitrogen into the threefold terrace site was achieved by fixing all the iron atoms in the surface slab, this way avoiding the relaxation of N into the fourfold site (i.e., at N-1). In this case we obtained $E_{ads} = -6.3$ eV and $E_s = -9.4$ eV.

Using a larger unit cell in our calculations would allow for stronger relaxations in the first iron layer. In this case, nitrogen in geometry N-1 could adsorb deeper into the adsorbant and the situation would resemble even more the adsorption of nitrogen into Fe(100), where the coordination of N is actually 5 (nitrogen is also bonded to the atom directly below). However, we did not pursue this possibility, as the simulation with unit cells having >100 iron atoms is computationally very demanding.

2. Adsorption of B

In the geometry B-1 in Fig. 4, the boron atom has quite a high coordination. Again, we have labeled the neighboring atoms with letters. The distances to the nearest-neighbor iron atoms are (a) 2.03, (b) 2.48, (c) 1.93, (d) 2.1, and (e) 2.13 Å. Distances to the iron atoms are now longer than in the case of nitrogen but the coordination is clearly higher. The bigger distance comes as no surprise, due to the higher orbital radius of boron atom when compared to nitrogen. In general, boron is also known to prefer high coordination.[78] The higher coordination preference of boron is more clearly observed in the adsorption geometry B-2. The iron step edge atoms are not as tightly bound as the terrace atoms and for this reason the strong reconstruction of iron atoms seen in B-2 is possible. There are now altogether six iron atoms surrounding the boron atom (one of them directly below the boron atom), all within a distance of 2.0–2.24 Å.

In the adsorption geometry B-3 the preference for high coordination of boron is again obvious but it is frustrated due to the lack of suitable sites. No strong reconstruction, like the one seen in geometry B-2 is observed because arranging the iron atoms in the close-packed region would be energetically very unfavorable. Boron cannot push itself very deeply into the iron layer either, the trick employed by nitrogen in N-1, as it has more extended orbital radii. The "frustration" of B-3 when compared to B-1 and B-2 is obvious in the energetics of Table I, as B-1 and B-2 are practically degenerate and B-3 resides 0.3 eV higher in energy.

3. Adsorption of N_2

Looking at the N-N bond length (BL) of geometry N_2-1 in Table I, we can see that it has been expanded by ~20%, which implies we are approaching dissociation. In Fig. 4 some of the neighboring iron atoms of the nitrogen atoms have been labeled with letters. The distances of the nitrogen atoms to their nearest iron neighbors are (a) 1.93, (b) 1.94, (e) 2.04 Å and (d) 1.9, (c) 1.95, (e) 2.12 Å. Similar to the case of an isolated nitrogen atom, nitrogen prefers a total coordination of four (i.e., surrounded by one nitrogen atom and three iron atoms). It is then not surprising that N_2 prefers the step edge; due to the morphology of the step edge, there are sites offering threefold coordination with iron for each one of the nitrogen atoms while maintaining a reasonable N-N bond length.

The adsorption geometry N_2-2 is very similar to N_2-1 and it has N-N bond length expanded by ~14%. Now the neighboring iron atoms move but very slightly; the distances a-c and b-d expand both only by ~4%. Each nitrogen atom is seen to have three iron neighbors. The nitrogen-iron nearest-neighbor distances for each nitrogen atom are (a) 2.09, (b) 1.89, (c) 2.07 Å and (a) 2.09, (d) 1.9, (c) 2.1 Å. Again, the nitrogen atom coordination is four (three iron atoms and one nitrogen atom). The geometry N_2-3 is very similar to N_2-1 and N_2-2 and the total energies for all adsorption geometries of N_2 molecule from Table I are almost degenerate. The step edge geometry N_2-1 is slightly more favorable than the others, as the nitrogen atoms can obtain their preferred coordination without significant rearrangement of the iron atoms.

Earlier calculations of N_2 adsorption on iron surface include Refs. 79 and 80. In Ref. 79, N_2 and N adsorption on the low-coordinated Fe(111) have been studied using DFT. In that reference, bigger N_2 concentrations (and smaller unit cells) were studied. In Ref. 80 the N_2 and N adsorption on Fe(110) were studied, using a 2×2 unit cell but in this study, the atoms of the iron slab were fixed. These earlier computational studies are therefore not directly comparable to the present work.

In both Refs. 79 and 80 the N_2 molecule was found to prefer the "top" site [i.e. site (1) in Fig. 2] and a geometry where the N-N bond projects into the vacuum (i.e. it is "standing" on the surface). We also find this same adsorption geometry [not shown in Fig. 4] to be a local minimum but its total energy is ≈0.6 eV higher than that of N_2-2 in Fig. 4. Keeping in mind that Ref. 79 emphasizes that N_2 adsorption geometries where both N atoms are in contact with the iron adsorbant are very dependent on the coverage and that the
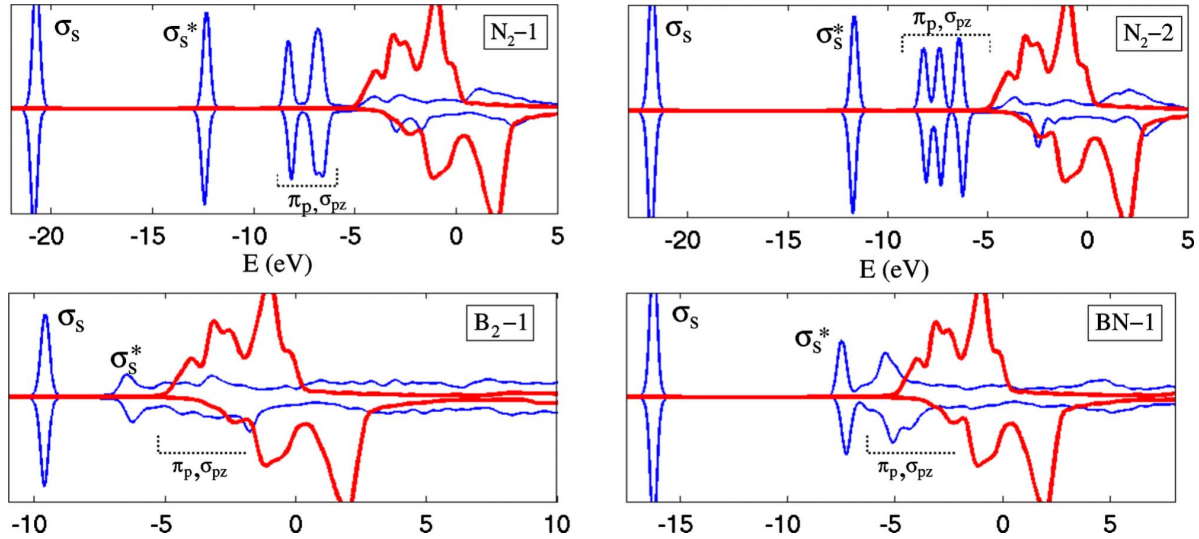
FIG. 6. (Color online) Density of states, projected into atom-centered iron *d* orbitals (thick red line) and into B and N atom-centered *s* and *p* orbitals (blue line). The states have been interpreted using the same notation as in Figs. 7 and 8. Peaks with significant *s*-orbital character only when projected to atom-centered B and N orbitals are most easily identified (σ_s and σ_s^*). Majority (positive values) and minority spin (negative values) are indicated.

coverage in our case is quite low, the result we have obtained is not surprising.

4. Adsorption of B_2

At first sight, the adsorption geometries of Fig. 4 for individual boron atoms and the B_2 molecule are very similar. The five nearest-neighbor iron atoms for a single boron atom in B_2-1 are within the range of 2.2–2.47 Å. The coordination of a single boron atom in B_2-1 is therefore between 4 and 5, which is very similar to the case of B-1. The bond length of B_2-1 has been expanded by 10%. The tendency for high coordination is more clear in geometry B_2-2 where a strong reconstruction of the iron layer, similar to the case of B-1, occurs. For one boron atom in B_2-2 the four nearest-neighbor iron atoms are within a range of 1.94–2.32 Å and the total coordination of a boron atom is then ~5 (i.e., four iron atoms and another boron atom).

In geometry B_2-3, one boron atom resides near a step edge and has a high coordination while the other boron is in the terrace region and cannot get high coordination. The boron atoms in B_2-4 have obtained high coordination through the reconstruction of the iron layer (the situation looks very similar to B_2-2) but on the other hand, there must be a high-energy cost for moving the iron layer atoms in the close-packed region. This can be seen in Table I, where B_2-4 lies 0.3 eV higher in energy than B_2-2.

5. Adsorption of BN

As we have discussed in previous sections, nitrogen and boron atoms prefer different coordination numbers. They maintain their preferences even when forming a molecule. In particular, nitrogen was seen to prefer threefold to fourfold coordination while boron prefers fivefold to sixfold coordination. In the case of boron nitride molecule, we should then find a suitable surface morphology that would allow simul-

taneously these different coordinations for boron and nitrogen. It is obvious that the step edge offers the best possibility for this.

Looking at Fig. 4 and Table I we observe that the most favorable adsorption sites for the boron nitride molecule are indeed at the step edge. Looking first at BN-1, we see that the bond length is almost equal to the free molecule, expanded only by ~4%. The nearest-neighbor iron atoms for
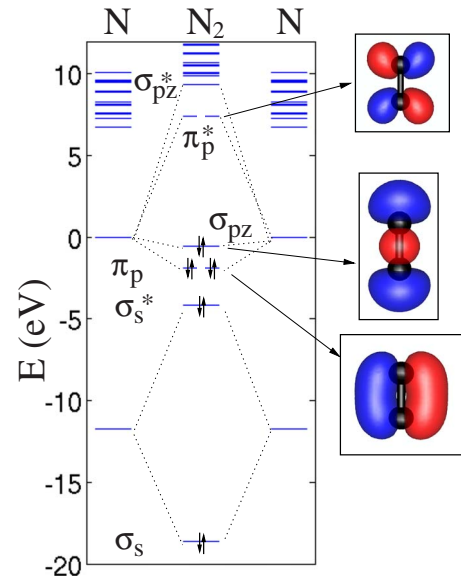

FIG. 7. (Color online) (Left) Energy level diagrams for individual N atoms and the N_2 molecule as calculated with VASP. N_2 energy levels are interpreted using the molecular-orbital theory. The net spin polarization of the N_2 molecule is zero, so including the electron spin in the calculations does not affect the results. Some one-electron states (from a SIESTA calculation) have been included in the insets: color red (blue) corresponds to positive (negative) values of the wave function.
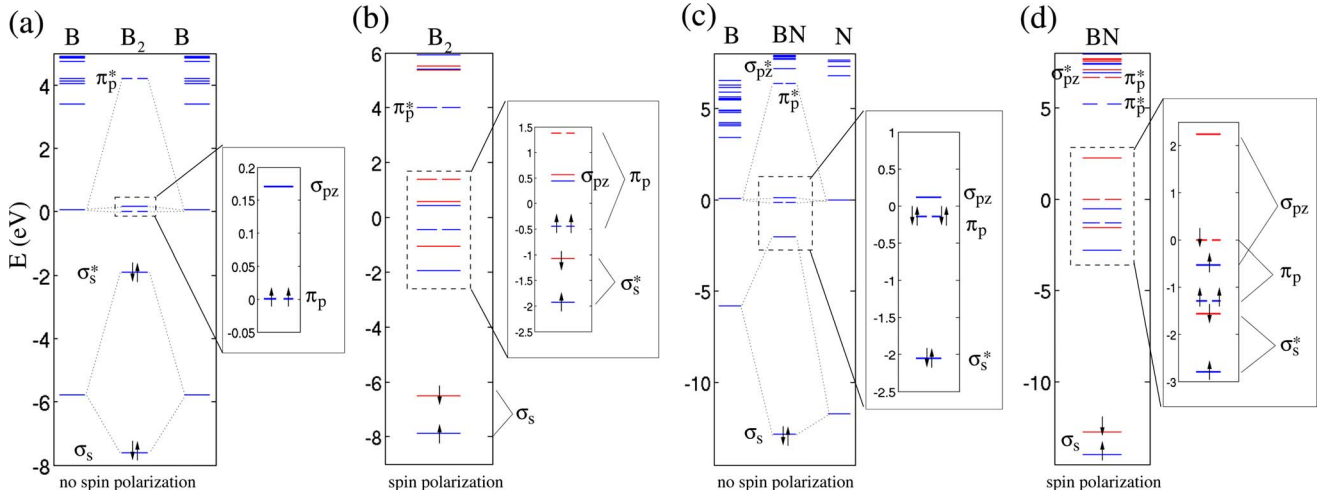
FIG. 8. (Color online) [(a) and (b)] Energy level diagrams for individual B atoms and the B_2 molecule as calculated with VASP (a) without and (b) with spin polarization. The B_2 energy levels are interpreted using the molecular-orbital theory. [(c) and (d)] Energy level diagrams for individual B and N atoms and the BN molecule as calculated with VASP (c) without and (d) with spin polarization. The BN energy levels are interpreted using the molecular-orbital theory. Blue (red) color corresponds to spin-up (down) states.

nitrogen are (c) 1.89, (d) 1.90, and (e) 2.25 Å while for boron they are (a) 1.97, (e) 2.1, (f) 2.31, and (d) 2.43 Å. Geometries BN-2 and BN-3 exhibit a very similar trend, i.e., the boron atom is higher coordinated than the nitrogen atom. The geometries BN-4 and BN-5 are almost degenerate in energy and "frustrated" because the molecule is not able to obtain coordination of 3–4 for nitrogen and 5–6 for boron due to the flat morphology of the terrace region.

C. Electronic structure of molecules on the catalyst

In this section we take a look at the electronic structure and bonding of molecules on the iron adsorbant. In particular, we are interested why B_2 and BN are stabilized on the surface while N_2 is so unstable. We do this by looking at the electronic states of the molecules in vacuum and at their density of states on the adsorbant.

A classical example of this kind of analysis is the Blyholder model for the CO molecule (see Ref. 81 and references therein), where the low-lying molecular orbitals (MOs) stay relatively inert while the MOs energetically near to the adsorbant d states or overlapping with them [most notably the highest occupied molecular orbital (HOMO) and lowest unoccupied molecular orbital (LUMO) states] dominate the chemisorption energies. Very related to our case is also the Norskov d-band model,[82–86] where the metal sp states broaden and shift the adsorbate states and these "renormalized" states are then hybridized with the metal d states. In our case, we will take a very "rough" look only into the density of states without looking at the exact details of the orbital mixing, which might be very complicated due to the strong atomic reconstruction of the topmost iron layer [see, for example, geometries N-1 and B-2 in Fig. 4]. In particular, we are interested in which type of orbitals of the adsorbate (bonding or antibonding) interact most strongly with the metal d states.

The iron atoms near the adsorbate are known to lower their magnetic moments while the adsorbate itself might be demagnetized or even obtain a minority spin.[76] This demagnetization can also be seen in the density of states of the adsorbates in Fig. 6.

1. Adsorption of N$_2$

The energy levels of N_2 are plotted in Fig. 7 and they are similar to earlier published ones.[87] We observe that N_2 is closed shell and that the energy difference between σ_{pz} (HOMO) and π_p^* (LUMO) is ~8 eV. The bond order of N_2 is 3 and there is no net spin magnetic moment. When N_2 is put in contact with an adsorbant, the bonding is likely dominated by the σ_{pz} and π_p^* states. From the electronegativity of nitrogen and iron, we could argue that N_2 is likely to receive electrons and thus bond through the antibonding state π_p^* (LUMO). To be more precise, this should depend on the relative position of the iron d states with respect to the renormalized N_2 energy levels, as mentioned earlier.

Comparing the projected density of states (PDOS) graphs of N_2-1 and N_2-2 in Fig. 6 to the energy diagram of Fig. 7, we can easily relate different peaks to the energy levels of the isolated N_2 molecule. In Fig. 6 the situation is most clear in the case of N_2-2, where we find altogether five N_2 peaks below the iron d states. Two of these peaks (almost degenerate) must correspond to π_p and one to σ_{pz}. There is no sign of a π_p^* peak, so it has likely hybridized with the iron d states. We can then conclude that N_2 is destabilized on the iron surface through adsorption using the antibonding π_p^* orbitals.

2. Adsorption of B$_2$

In Fig. 8 we have plotted the energy levels of a single boron atom and the energy levels of the B_2 molecule. We observe that B_2 has an open shell structure. The energy difference between π_p (HOMO) and σ_{pz} (LUMO) is ~160 meV. The bond order is 1 and B_2 has a net magnetic moment of $2\mu_B$. When the calculation includes spin polar-

ization, an exchange splitting of the energy levels is observed and the degeneracy of π_p orbital is removed. Including spin polarization in the calculation, lowers the energy of the B_2 molecule by 0.84 eV.

The adsorption of B_2 is likely to happen through π_p and σ_{pz} orbitals, as the gap between them is very small. Both of these orbitals are of bonding type and this implies that B_2 will be stabilized upon adsorption. Looking at PDOS of B_2, when it has been placed on the iron surface [B_2-1 in Fig. 6], we see that both the π_p and σ_{pz} MOs overlap with the iron d states and the peaks corresponding to these MOs have hybridized with the iron d states. The stabilization of B_2 on iron then looks natural in the light of the electronic structure. Something reminiscent of an exchange splitting in the adsorbate PDOS peaks can be seen in the energy range from ~-4 to -1 eV.

3. Adsorption of BN

In Fig. 8 we have plotted the energy levels of boron and nitrogen atoms together with the levels of the BN molecule. In a calculation without electron spin, the situation looks straightforward and the BN molecule has a closed-shell structure with π_p (HOMO) and σ_{pz} (LUMO) having a gap of ~250 meV. The bond order is 2 and there is no net spin magnetic moment. When spin polarization is allowed, a considerable rearrangement of the MOs due to the exchange splitting takes place: π_p and σ_{pz} orbitals slide through each other in the energy-level diagram (π_p "down" states shift upward, while σ_{pz} "up" states shift down) and one of the σ_{pz} states becomes occupied. BN molecule lowers its energy by 0.36 eV and obtains a net magnetic moment of $2\mu_B$.

It is very difficult to anticipate which one of the orbitals, π_p or σ_{pz}, will dominate the adsorption, as they are very close to each other in energy. Magnetism makes this situation even more complicated, as the gap between these molecular orbitals can close up due to the exchange splitting. Both of these orbitals are of the bonding type, so at least BN should be stabilized on the adsorbant. We look again at the PDOS plots of Fig. 8 and identify the peaks with the energy levels of Fig. 6. We can see that both the π_p and σ_{pz} states coincide with the iron d states and hybridize with them. There are even some slight traces of the exchange splitting in the adsorbate PDOS peaks. Finally, we will try to explain by means of the electronic structure only, why B_2 is more stable on iron than BN.

The HOMO (π_p) and LUMO (σ_{pz}) states for an isolated B_2 molecule in Fig. 8(a) lie at energies of 0.0 and ~0.18 eV while for BN in Fig. 8(c) they lie at ~-0.15 and ~0.12 eV. The HOMO and LUMO states of the BN molecule are then shifted slightly downward, when compared to the same states of the B_2 molecule. These states are then energetically closer to the iron d states in B_2 than in BN. Supporting this idea, when looking at Fig. 6 and comparing B_2-1 and BN-1, we can see that the hybridization of the π_p and σ_{pz} states with the iron d states seems to be more pronounced in the case of B_2 and this implies that the adsorption through these bonding-type orbitals is stronger.

V. DISCUSSION AND CONCLUSIONS

We have performed an *ab initio* study of the energetics of the simplest chemical reactions involved in catalytic growth of BNNTs. We studied adsorbed boron and nitrogen atoms (N^*,B^*) and all their adsorbed diatomic combinations (N_2^*, B_2^*, and BN^*) on an iron catalyst.

Our objective was to study the fundamental aspect of BN bond stabilization on iron [rather than modeling realistic reaction conditions, see Sec. II F]. In order to do this, we mimicked the very first stages of a CVD synthesis of BN structures. We assumed that precursors (without defining them) have dissociated and donated individual adsorbed N and B atoms on the catalyst. In the very first stages of the synthesis, these atoms start to form either adsorbed N_2, B_2, or BN molecules. We believe that understanding when the BN bond is stabilized can provide help in understanding the BNNT synthesis in general. Specifically, we observed that N_2 is unstable while B_2 and BN are stabilized on the iron catalyst (BN only at the step edge region). N_2 dissociates by adsorption on iron through antibonding orbitals while B_2 and BN are stabilized by dominant adsorption through bonding-type orbitals.

Apart from simply studying the energetics and stabilization of the BN molecule we can also speculate how the energies and reaction barriers for BN molecule formation could affect the synthesis. In order to do this, we must assume an intermediate step for the initiation of BNNT growth. As mentioned in Sec. II F, the formation mechanisms of BNNTs can be extremely complex. If we assume that the intermediate step of creating a large number of BN molecules is a prerequisite in initiating the BNNT formation, then situations where formation of BN molecules are favored over other competing reactions are desirable for the synthesis (these molecules should also remain mobile and not poison the catalyst). It seems intuitive that some sort of boron nitride nucleus is needed to initiate further BN structure growth and that for the formation of this nucleus a large number of BN molecules is required. Other pathways for the initiation of BNNT growth seem to be less intuitive (of course, not impossible) than the one we are considering here; it is difficult to see how a nanotube could form, for example, from an amorphous boron cluster, at least without using very high temperatures (for example, in the case of boron clusters, as mentioned in Sec. II, BNNT growth from boron has been observed only in very elevated temperatures).

On terrace regions of the iron catalyst, the reaction forming B_2 is exothermic while the reaction forming BN is slightly endothermic. The energy barriers of the two competing reactions $B^*+B^* \rightarrow B_2^*$ and $B^*+N^* \rightarrow BN^*$ are the same order of magnitude for the two reactions (i.e., they do not play a critical role in defining the reaction product). This implies that if B and N atoms are distributed on a flat iron surface, in the very first stages of the synthesis, both (a) adsorbed B_2 and adsorbed nitrogen atoms and (b) adsorbed BN molecules will form. According to our calculations, forming (a) B_2 (−0.4 eV) is slightly more favorable than forming (b) BN (0.1 eV). As explained above and assuming that BN molecule formation is important for BNNT synthesis, this situation is undesirable.

The situation looks more promising at the step edge; now both reactions are exothermic and the energetic balance is tipped into favor of BN formation (−0.1 eV for B_2 and −0.3 eV for BN). The energy barriers are again the same

magnitude for both reactions $B^*+B^* \rightarrow B_2^*$ and $B^*+N^* \rightarrow BN^*$. This implies that when B and N atoms are distributed into the step edge, some more BN than B_2 molecules should form (at least when compared to the flat surface case). The stabilization of BN at the step edge can be explained in terms of atomic coordination: we observed that, within the computational unit cell we used, nitrogen preferred threefold to fourfold while boron fivefold to sixfold coordination with iron and the only morphology where these two coordinations are simultaneously available, is found at the step edge.

Finally, one must be cautious in drawing very definite conclusions with respect to possible BNNT synthesis on iron catalyst based on our results: we have assumed a certain (although intuitive) reaction path for BNNT growth initiation (formation of large number of BN molecules) and that the energetic stability of this step is important (when compared to kinetics), we have not considered realistic reaction conditions and the energy differences for competing reactions are quite small (in the range of hundreds of meV).

Summarizing, according to our calculations, the BN bond is stabilized in step edge regions of the iron catalyst. This implies that the yield of BNNT in a CVD synthesis might be enhanced by altering the iron catalyst morphology to include more steps, instead of close-packed surface regions. Simply having step edges is not enough; having step edges, but long terraces, will result in more flat surface sites than step edge sites, lowering the free energy for flat surface sites. From the point of view of maximizing the BNNT yield, the terraces should then be very short. As creating a catalyst nanoparticle with a desired morphology is very difficult, the predictions on BN yield given in this theoretical work could be put to test in practice by using as a catalyst a high-index Fe surface with very short steps.

ACKNOWLEDGMENTS

---

*sampsa.riikonen@iki.fi

[1] N. G. Chopra, R. J. Luyken, K. Cherrey, V. H. Crespi, M. L. Cohen, S. G. Louie, and A. Zettl, Science **269**, 966 (1995).

[2] D. Golberg, Y. Bando, M. Eremets, K. Takemura, K. Kurashima, and H. Yusa, Appl. Phys. Lett. **69**, 2045 (1996).

[3] A. Rubio, J. L. Corkill, and M. L. Cohen, Phys. Rev. B **49**, 5081 (1994).

[4] E. Hernández, C. Goze, P. Bernier, and A. Rubio, Phys. Rev. Lett. **80**, 4502 (1998).

[5] X. Blase, A. Rubio, S. G. Louie, and M. L. Cohen, Europhys. Lett. **28**, 335 (1994).

[6] J.-C. Charlier, A. De Vita, X. Blase, and R. Car, Science **275**, 647 (1997).

[7] R. T. Paine and C. K. Narula, Chem. Rev. (Washington, D.C.) **90**, 73 (1990).

[8] C. Tang and Y. Bando, Appl. Phys. Lett. **83**, 659 (2003).

[9] D. Golberg, Y. Bando, C. Tang, and C. Zhi, Adv. Mater. **19**, 2413 (2007).

[10] N. Grobert, Mater. Today **10**, 28 (2007).

[11] M. Terranova, V. Sessa, and M. Rossi, Chem. Vap. Deposition **12**, 315 (2006).

[12] J.-Y. Raty, F. Gygi, and G. Galli, Phys. Rev. Lett. **95**, 096103 (2005).

[13] F. Abild-Pedersen, J. K. Nørskov, J. R. Rostrup-Nielsen, J. Sehested, and S. Helveg, Phys. Rev. B **73**, 115419 (2006).

[14] H. Amara, J.-M. Roussel, C. Bichara, J.-P. Gaspard, and F. Ducastelle, Phys. Rev. B **79**, 014109 (2009).

[15] A. Loiseau, F. Willaime, N. Demoncy, G. Hug, and H. Pascard, Phys. Rev. Lett. **76**, 4737 (1996).

[16] M. Terrones, W. K. Hsu, H. Terrones, J. P. Zhang, S. Ramos, J. P. Hare, R. Castillo, K. Prassides, A. K. Cheetham, H. W. Kroto, and D. R. M. Walton, Chem. Phys. Lett. **259**, 568 (1996).

[17] J. Cumings and A. Zettl, Chem. Phys. Lett. **316**, 211 (2000).

[18] A. M. Morales and C. M. Lieber, Science **279**, 208 (1998).

[19] Z. G. Wen, Z. Ze, B. Z. Gang, and Y. D. Peng, Solid State Commun. **109**, 555 (1999).

[20] D. P. Yu, X. S. Sun, C. S. Lee, I. Bello, S. T. Lee, H. D. Gu, K. M. Leung, G. W. Zhou, Z. F. Dong, and Z. Zhang, Appl. Phys. Lett. **72**, 1966 (1998).

[21] R. S. Lee, J. Gavillet, M. LamydelaChapelle, A. Loiseau, J.-L. Cochon, D. Pigache, J. Thibault, and F. Willaime, Phys. Rev. B **64**, 121405 (2001).

[22] R. Arenal, O. Stephan, J.-L. Cochon, and A. Loiseau, J. Am. Chem. Soc. **129**, 16183 (2007).

[23] T. Laude, Y. Matsui, A. Marraud, and B. Jouffrey, Appl. Phys. Lett. **76**, 3239 (2000).

[24] D. Golberg, A. Rode, Y. Bando, M. Mitome, E. Gamaly, and B. Luther-Davies, Diamond Relat. Mater. **12**, 1269 (2003).

[25] S. Y. Bae, H. W. Seo, J. Park, Y. S. Choi, J. C. Park, and S. Y. Lee, Chem. Phys. Lett. **374**, 534 (2003).

[26] Y. Chen, L. T. Chadderton, J. F. Gerald, and J. S. Williams, Appl. Phys. Lett. **74**, 2960 (1999).

[27] Y. Chen, J. F. Gerald, J. S. Williams, and S. Bulcock, Chem. Phys. Lett. **299**, 260 (1999).

[28] J. Velázquez-Salazar, E. Munoz-Sandoval, J. Romo-Herrera, F. Lupo, M. Rühle, H. Terrones, and M. Terrones, Chem. Phys. Lett. **416**, 342 (2005).

[29] J. Yu, Y. Chen, R. Wuhrer, Z. Liu, and S. Ringer, Chem. Mater. **17**, 5172 (2005).

[30] J. Yu, B. C. P. Li, J. Zou, and Y. Chen, J. Mater. Sci. **42**, 4025 (2007).

[31] H. Tokoro, S. Fujii, and T. Oku, Diamond Relat. Mater. **13**, 1139 (2004).

[32] N. Koi, T. Oku, and M. Nishijima, Solid State Commun. **136**, 342 (2005).

[33] T. Oku, N. Koi, K. Suganuma, R. V. Belosludov, and Y. Kawa-

zoe, Solid State Commun. **143**, 331 (2007).

[34] I. Narita, T. Oku, H. Tokoro, and K. Suganuma, J. Electron Microsc. **55**, 123 (2006).

[35] P. Gleize, M. C. Schouler, P. Gadelle, and M. Caillet, J. Mater. Sci. **29**, 1575 (1994).

[36] K. Shelimov and M. Moskovits, Chem. Mater. **12**, 250 (2000).

[37] O. Lourie, C. Jones, B. Bartlett, P. Gibbons, R. Ruoff, and W. Buhro, Chem. Mater. **12**, 1808 (2000).

[38] R. Ma, Y. Bando, and T. Sato, Chem. Phys. Lett. **337**, 61 (2001).

[39] K. F. Huo, Z. Hu, F. Chen, J. J. Fu, Y. Chen, B. H. Liu, J. Ding, Z. L. Dong, and T. White, Appl. Phys. Lett. **80**, 3611 (2002).

[40] C. Tang, Y. Bando, and T. Sato, Chem. Phys. Lett. **362**, 185 (2002).

[41] J. J. Fu, Y. N. Lu, H. Xu, K. F. Huo, X. Z. Wang, L. Li, Z. Hu, and Y. Chen, Nanotechnology **15**, 727 (2004).

[42] R. Ma, Y. Bando, T. Sato, and K. Kurashima, Chem. Mater. **13**, 2965 (2001).

[43] T. S. R. Ma and Y. Bando, Adv. Mater. **14**, 366 (2002).

[44] A. Nagashima, N. Tejima, Y. Gamou, T. Kawai, and C. Oshima, Phys. Rev. Lett. **75**, 3918 (1995).

[45] W. Han, Y. Bando, K. Kurashima, and T. Sato, Appl. Phys. Lett. **73**, 3085 (1998).

[46] W. Han, P. Redlich, F. Ernst, and M. Rühle, Appl. Phys. Lett. **75**, 1875 (1999).

[47] D. Golberg, Y. Bando, W. Han, K. Kurashima, and T. Sato, Chem. Phys. Lett. **308**, 337 (1999).

[48] D. Golberg, Y. Bando, K. Kurashima, and T. Sato, Chem. Phys. Lett. **323**, 185 (2000).

[49] X. Chen, X. Wang, J. Liu, Z. Wang, and Y. Qian, Appl. Phys. A: Mater. Sci. Process. **81**, 1035 (2005).

[50] F. L. Deepak, C. P. Vinod, K. Mukhopadhyay, A. Govindaraj, and C. N. R. Rao, Chem. Phys. Lett. **353**, 345 (2002).

[51] C. Tang, Y. Bando, T. Sato, and K. Kurashima, Chem. Commun. (Cambridge) 2002, 1290.

[52] C. Zhi, Y. Bando, C. Tan, and D. Golberg, Solid State Commun. **135**, 67 (2005).

[53] C. Guo and P. M. Kelly, Mater. Sci. Eng., A **352**, 40 (2003).

[54] J.-C. Charlier, X. Blase, A. D. Vita, and R. Car, Appl. Phys. A: Mater. Sci. Process. **68**, 267 (1999).

[55] J. K. Nørskov, T. Bligaard, A. Logadóttir, S. Bahn, L. B. Hansen, M. Bollinger, H. Bengaard, B. Hammer, Z. Sljivancanin, M. Mavrikakis, Y. Xu, S. Dahl, and C. J. H. Jacobsen, J. Catal. **209**, 275 (2002).

[56] K. Honkala, A. Hellman, I. N. Remediakis, A. Logadóttir, A. Carlsson, S. Dahl, C. H. Christensen, and J. K. Nørskov, Science **307**, 555 (2005).

[57] P. Stoltze and J. K. Nørskov, Phys. Rev. Lett. **55**, 2502 (1985).

[58] A. Logadóttir and J. K. Nørskov, J. Catal. **220**, 273 (2003).

[59] J. M. Soler, E. Artacho, J. D. Gale, A. García, J. Junquera, P. Ordejón, and D. Sánchez-Portal, J. Phys.: Condens. Matter **14**, 2745 (2002).

[60] D. Sánchez-Portal, P. Ordejón, E. Artacho, and J. M. Soler, Int. J. Quantum Chem. **65**, 453 (1997).

[61] G. Kresse and J. Hafner, Phys. Rev. B **47**, 558 (1993).

[62] G. Kresse and J. Furthmüller, Phys. Rev. B **54**, 11169 (1996).

[63] G. Kresse and D. Joubert, Phys. Rev. B **59**, 1758 (1999).

[64] P. E. Blöchl, Phys. Rev. B **50**, 17953 (1994).

[65] J. P. Perdew, K. Burke, and M. Ernzerhof, Phys. Rev. Lett. **77**, 3865 (1996).

[66] H. J. Monkhorst and J. D. Pack, Phys. Rev. B **13**, 5188 (1976).

[67] G. Henkelman, B. P. Uberuaga, and H. Jónsson, J. Chem. Phys. **113**, 9901 (2000).

[68] N. Troullier and J. L. Martins, Phys. Rev. B **43**, 1993 (1991).

[69] E. Artacho, D. Sánchez-Portal, P. Ordejón, A. García, and J. M. Soler, Phys. Status Solidi B **215**, 809 (1999).

[70] J. Junquera, O. Paz, D. Sánchez-Portal, and E. Artacho, Phys. Rev. B **64**, 235111 (2001).

[71] O. F. Sankey and D. J. Niklewski, Phys. Rev. B **40**, 3979 (1989).

[72] J. Izquierdo, A. Vega, L. C. Balbás, D. Sánchez-Portal, J. Junquera, E. Artacho, J. M. Soler, and P. Ordejón, Phys. Rev. B **61**, 13639 (2000).

[73] A. Postnikov, P. Entel, and J. Soler, Eur. Phys. J. D **25**, 261 (2003).

[74] M. Methfessel and A. T. Paxton, Phys. Rev. B **40**, 3616 (1989).

[75] C. Kittel, *Introduction to Solid State Physics*, 6th ed. (Wiley, New York, 1986).

[76] S. J. Jenkins, Q. Ge, and D. A. King, Phys. Rev. B **64**, 012413 (2001).

[77] J. J. Mortensen, M. V. Ganduglia-Pirovano, L. B. Hansen, B. Hammer, P. Stoltze, and J. K. Nørskov, Surf. Sci. **422**, 8 (1999).

[78] I. Boustani, Phys. Rev. B **55**, 16426 (1997).

[79] J. J. Mortensen, L. B. Hansen, B. Hammer, and J. K. Nørskov, J. Catal. **182**, 479 (1999).

[80] A. Logadottir and J. K. Nørskov, Surf. Sci. **489**, 135 (2001).

[81] P. Hu, D. A. King, M. H. Lee, and M. C. Payne, Chem. Phys. Lett. **246**, 73 (1995).

[82] B. Hammer and J. K. Nørskov, Nature (London) **376**, 238 (1995).

[83] B. Hammer and J. K. Nørskov, Surf. Sci. **343**, 211 (1995).

[84] B. Hammer, Y. Morikawa, and J. K. Nørskov, Phys. Rev. Lett. **76**, 2141 (1996).

[85] B. Hammer, O. H. Nielsen, and J. K. Nørskov, Catal. Lett. **46**, 31 (1997).

[86] B. Hammer, Top. Catal. **37**, 3 (2006).

[87] R. Stowasser and R. Hoffmann, J. Am. Chem. Soc. **121**, 3414 (1999).